bioRxiv preprint doi: https://doi.org/10.1101/743237; this version posted August 22, 2019. The copyright holder for this preprint (which was not certified by peer review) is the author/funder, who has granted bioRxiv a license to display the preprint in perpetuity. It is made available under aCC-BY 4.0 International license.

Inhibition of a negative feedback for persistent epithelial cell–cell junction contraction by p21-activated kinase 3

Authors: Hiroyuki Uechi and Erina Kuranaga*

Affiliations: Laboratory for Histogenetic Dynamics, Graduate School of Life Sciences, Tohoku University, 6-3, Aramaki-aza-aoba, Aoba-ku, Sendai 980-8578, Japan

*Corresponding author (erina.kuranaga.d1@tohoku.ac.jp)

bioRxiv preprint doi: https://doi.org/10.1101/743237; this version posted August 22, 2019. The copyright holder for this preprint (which was not certified by peer review) is the author/funder, who has granted bioRxiv a license to display the preprint in perpetuity. It is made available under aCC-BY 4.0 International license.

Abstract

Actin-mediated mechanical forces are central drivers of cellular dynamics. They generate protrusive and contractile dynamics, the latter of which are induced in concert with myosin II bundled at the site of contraction. These dynamics emerge concomitantly in tissues and even each cell; thus, the tight regulation of such bidirectional forces is important for proper cellular deformation. Here, we show that contractile dynamics can eventually disturb cell–cell junction contraction in the absence of p21-activated kinase 3 (Pak3). Upon Pak3 depletion, contractility induces the formation of abnormal actin protrusions at the shortening junctions, which reduces E-cadherin levels at adherens junctions. Such E-cadherin dilution dissociates myosin II from the contracting junctions, leading to a reduction in junctional tensile forces. Overexpressing E-cadherin restores the association of myosin II at the junctions and junction contraction. Our results suggest that contractility both induces and perturbs junction contraction and that the attenuation of such perturbations by Pak3 facilitates persistent junction shortening.

bioRxiv preprint doi: https://doi.org/10.1101/743237; this version posted August 22, 2019. The copyright holder for this preprint (which was not certified by peer review) is the author/funder, who has granted bioRxiv a license to display the preprint in perpetuity. It is made available under aCC-BY 4.0 International license.

The cell collectives composing animal bodies sculpt tissue architectures through various cellular behaviors such as cell division, deformation, rearrangement, and migration. The cytoskeletal protein actin is the central protein that drives these cellular behaviors by generating mechanical forces[1–7]. While actin generates protrusive forces by forming branched and bundled structures, it also supplies contractile forces by forming bundled structures and loosely organized networks in concert with non-muscle myosin II. Such bidirectional force generation by actin can coexist in each cell and even at the same position within cells. During single-cell migration, protrusive actin dynamics extend cells at the leading edge, while actomyosin (the actin and myosin II complex) contraction causes retraction at the rear of the cell along the migrating direction[8,9]. A recent study of *Drosophila* eye development demonstrated that pulsatile extension by protrusive branched actin networks and counterbalancing actomyosin contractility-mediated shortening of each cell–cell contact control cellular shape[10]. Thus, the tight regulation of actin dynamics is important for proper force induction and the resultant cellular dynamics.

Epithelial cell intercalation is one of the multicellular dynamics driven by the contractile forces of actomyosin and contributes to directional tissue extension and movement[11–13]. This process consists of the directional exchange of cellular positions within

bioRxiv preprint doi: https://doi.org/10.1101/743237; this version posted August 22, 2019. The copyright holder for this preprint (which was not certified by peer review) is the author/funder, who has granted bioRxiv a license to display the preprint in perpetuity. It is made available under aCC-BY 4.0 International license.

cell collectives, which is driven by cell–cell junction remodeling (i.e., shortening of cell–cell junctions and subsequent growth of new ones in new directions)[14]. During shortening, actin and myosin II are highly enriched at the adherens junctions (AJs) of cell–cell junctions to form contractile actomyosin bundles that then shorten the junctions[1,11,15–19]. The mechanisms inducing contractile forces via actomyosin are well studied; however, it is still unknown whether actomyosin-mediated contractions are negatively affected during cell–cell junction shortening, and if so, how the shortening is sustained.

The rotation of *Drosophila* male genitalia is an example of epithelial cell intercalation[20]. During metamorphosis, male genitalia located at the posterior end of the body undergo 360° dextral rotation around the anterior–posterior axis (Fig. 1a)[21,22]. This rotation is observed from 24 to 36 h after puparium formation (APF), and is composed of two movements of epithelial cells: the initial 180° dextral movement of the genitalia along with the surrounding epithelia, which is called the posterior compartment of the A8 segment (A8p), at the anterior side of the genitalia, and the subsequent 180° dextral movement of the anterior compartment of the A8 segment (A8a), the latter of which starts at 26 h APF[20–22]. During rotation, the A8a cells frequently induce left–right polarized junction remodeling in relation to the anterior–posterior axis in the confined space between the A8p epithelia and the A7 segment, which

bioRxiv preprint doi: https://doi.org/10.1101/743237; this version posted August 22, 2019. The copyright holder for this preprint (which was not certified by peer review) is the author/funder, who has granted bioRxiv a license to display the preprint in perpetuity. It is made available under aCC-BY 4.0 International license.

61 results in unidirectional epithelial cell movement[20,23]. Consistent with other tissues, the
62 accumulation of actomyosin at the AJs of cell–cell junctions induces junction contraction in
63 this model. Down-regulation of contractile activity, such as via RNA interference (RNAi) of
64 myosin II regulatory light chain (MRLC), compromises the remodeling and hence results in
65 insufficient A8a cell movement, leading to incomplete rotation of the genitalia[20].

66 Here, we examined actin and myosin II dynamics in the A8a epithelia during the
67 rotation of *Drosophila* genitalia and revealed that, upon junction contraction, actin dynamics
68 at cell–cell junctions are compromised in p21-activated kinase 3 (Pak3) mutant flies. These
69 aberrant actin dynamics disturb the distribution of E-cadherin and myosin II at the junctions,
70 and thus eventually disrupt the junction contraction. These findings suggest that Pak3 blocks
71 the negative feedback of contractility and ensures persistent junction contraction and
72 rearrangement of epithelial cells.

73

74 **Results**

75 **Pak3 is required for A8a cell movement during the rotation of *Drosophila* genitalia.** To
76 understand the molecular basis underlying epithelial cell–cell junction remodeling, we
77 searched for genes involved in the movement of A8a cells. In the control flies, time-lapse

bioRxiv preprint doi: https://doi.org/10.1101/743237; this version posted August 22, 2019. The copyright holder for this preprint (which was not certified by peer review) is the author/funder, who has granted bioRxiv a license to display the preprint in perpetuity. It is made available under aCC-BY 4.0 International license.

images showed that male genitalia underwent the 360° full rotation during metamorphosis, and all male flies had the normal orientation of genitalia (Fig. 1a,b). We found that RNAi targeting Pak3 in the A8a epithelia under the control of the *AbdB-Gal4* driver caused insufficient movement of the A8a epithelia during rotation, while the genitalia still underwent the 180° movement with respect to the A8a epithelia (Fig. 1a)[24,25]. In addition, depleting Pak3 induced the misorientation of genitalia in approximately 60% of adult male flies, similar to that reported for MRLC depletion (Fig. 1b)[20]. Co-expression of Dicer2, which augments RNAi efficiency[26], with Pak3 RNAi increased the frequency of misorientation to > 90%, which was associated with a decline in rotation angle, while the overexpression (OE) of Pak3 tagged with green fluorescent protein (Pak3::GFP) restored the normal orientation, excluding the possibility of an off-target effect of this Pak3 RNAi (Fig. 1b). These results indicate that Pak3 is involved in epithelial tissue dynamics.

Immunostaining of fixed epithelia revealed that Pak3 was expressed in the A8a cells, as indicated by its decreased signals in Pak3 RNAi cells that were clonally introduced into wild-type tissues (Fig. 1c). Signals for the lateral membrane-associating protein Discs large (Dlg)[27] at cell–cell boundaries were indistinguishable between wild-type cells and Pak3 RNAi clones, suggesting that Pak3 RNAi does not compromise the integrity of epithelial cells (Fig.

bioRxiv preprint doi: https://doi.org/10.1101/743237; this version posted August 22, 2019. The copyright holder for this preprint (which was not certified by peer review) is the author/funder, who has granted bioRxiv a license to display the preprint in perpetuity. It is made available under aCC-BY 4.0 International license.

1c).

Pak3 is required for cell–cell junction shortening. To examine the role of Pak3 in cellular dynamics, we monitored the dynamics of cell–cell junctions labeled with GFP-tagged E-cadherin (E-Cad::GFP), an adhesive AJ component, during A8a cell movement[28,29]. In the control epithelia, we observed that cell–cell junctions undergo shortening, form four-way vertices, and subsequently grow in other directions, consistent with a previous report (Fig. 1d; Supplementary Movie 1)[20]. In the Pak3-depleted A8a cells, junctions frequently failed to complete shortening; that is, they did not shorten sufficiently to form four-way vertices and instead went back to the original direction (Fig. 1d; Supplementary Movie 2). To quantify these defective junction dynamics, we categorized the junctions in A8a cells according to their dynamics as follows: junctions that completed shortening and grew in other directions (remodeling), junctions that completed shortening, but failed to grow in other directions after forming four-way vertices (growth defect), junctions that shortened sufficiently to reach 1.5 μm in length, but failed to form four-way vertices (shortening defect), and junctions that did not shorten to less than 1.5 μm in length (no remodeling) (Fig. 1e). Then, the populations of junctions in each category were examined. In the control cells, approximately 55% of junctions

bioRxiv preprint doi: https://doi.org/10.1101/743237; this version posted August 22, 2019. The copyright holder for this preprint (which was not certified by peer review) is the author/funder, who has granted bioRxiv a license to display the preprint in perpetuity. It is made available under aCC-BY 4.0 International license.

112 underwent remodeling, and few junctions showed defects during a 4-h period following the
113 initiation of A8a cell movement (from 26 to 30 h APF, Fig. 1f). By contrast, in Pak3 RNAi
114 cells, the frequency of junction remodeling was decreased to < 10%, and instead, the number
115 of shortening junctions that failed to form four-way vertices (categorized as a shortening
116 defect) was significantly increased (Fig. 1f). Similar propensities were observed in the A8a
117 cells of a Pak3 hypomorphic mutant (*Pak3*^{d02472})[30], although the decline in remodeling
118 frequency was not substantial compared to that in Pak3 RNAi cells (Fig. 1f). Meanwhile, the
119 frequency of the growth defect was not altered in these Pak3 mutants (Fig. 1f). These results
120 suggest that Pak3 is required for junction shortening during cell intercalation.
121
122 **Pak3 suppresses aberrant actin dynamics in response to junction contraction.** Junction
123 shortening is driven by the contractile forces of actomyosin accumulating at the AJs of
124 junctions, and Pak protein families are known to regulate actin dynamics[5,31–33]. These findings
125 and our observations led us to speculate that Pak3 has roles in actin dynamics during junction
126 shortening in the A8a epithelia. To test this possibility, we performed time-lapse imaging of
127 GFP-tagged Lifeact (Lifeact::GFP), which labels F-actin[34]. In the control A8a cells, actin was
128 distributed predominantly at cell–cell junctions (Fig. 2a; Supplementary Movie 3). Magnified

bioRxiv preprint doi: https://doi.org/10.1101/743237; this version posted August 22, 2019. The copyright holder for this preprint (which was not certified by peer review) is the author/funder, who has granted bioRxiv a license to display the preprint in perpetuity. It is made available under aCC-BY 4.0 International license.

129 images showed that, whereas the majority of Lifeact::GFP signals were localized along
130 junctions, actin frequently generated small protrusions arising from the junctions (Fig. 2b). The
131 maximum size of these actin-positive protrusions was 1.1 ± 0.34 μm in height (perpendicular
132 to the junctions) and 2.1 ± 1.1 μm in width (parallel to the junctions) (Fig. 2c). These
133 observations suggest that actin not only merely forms into bundled structures along cell–cell
134 junctions but also generates small protrusive structures in the A8a cells undergoing junction
135 remodeling. In Pak3 RNAi cells, actin also localized to cell–cell junctions, but generated
136 significantly larger protrusive structures, compared to those in the control cells (Fig. 2a–c;
137 Supplementary Movie 4). Similar actin-positive structures were also observed in *Pak3*^{d02472}
138 flies with another actin-labeling probe, GFP-tagged actin-binding domain of utrophin
139 (UtrABD::GFP) (Fig. 2d)[35,36]. To semi-quantify these actin dynamics in Pak3 RNAi cells, we
140 defined a "large" actin protrusion as a Lifeact-positive cluster at junctions that was greater than
141 1.5 μm in height and greater than 3 μm in width in a planar section; both lengths approximately
142 exceeded the mean + 1 standard deviation (S.D.) of each length of the actin protrusions in the
143 control cells, respectively (Fig. 2c,e). We then examined the frequency of the appearance of
144 such large protrusions at each junction (Fig. 2f). While greater than 95% of cell–cell junctions
145 in the control cells did not generate large protrusions, these structures emerged at almost all

bioRxiv preprint doi: https://doi.org/10.1101/743237; this version posted August 22, 2019. The copyright holder for this preprint (which was not certified by peer review) is the author/funder, who has granted bioRxiv a license to display the preprint in perpetuity. It is made available under aCC-BY 4.0 International license.

146 junctions at least once per hour in Pak3 RNAi cells (Fig. 2f). Again, overexpressing Pak3
147 partially alleviated the formation of large protrusions: although these structures were still
148 observed in approximately 50% of junctions, they were absent from greater than 40% of
149 junctions, and only a few junctions formed large protrusions more than three times per hour
150 (Fig. 2f). These data suggest that Pak3 suppresses the formation of aberrant actin protrusions
151 in the A8a cells.

152 Branched actin networks induce the formation of protrusive actin structures and are
153 generated by the Arp2/3 complex, which is stimulated by the WAVE regulatory complex
154 (WRC)[1,3]. To determine whether this pathway is involved in the formation of large protrusions,
155 we used RNAi targeting Abi, a component of the WRC, in Pak3-depleted cells[37,38]. Depletion
156 of Abi suppressed the generation of large actin protrusions, although it did not completely
157 restore actin dynamics (Fig. 2f). This suggests that the aberrant actin protrusions are in part
158 composed of branched actin-networks.

159 To further characterize these aberrant actin protrusions in Pak3 RNAi cells, we
160 explored the correlation between their emergence and junction dynamics. In Pak3-depleted
161 cells, junctions failed to undergo remodeling (Fig. 1f), but instead underwent repeated
162 shrinkage and extension (Fig. 2g). We found that the generation of large protrusions was

bioRxiv preprint doi: https://doi.org/10.1101/743237; this version posted August 22, 2019. The copyright holder for this preprint (which was not certified by peer review) is the author/funder, who has granted bioRxiv a license to display the preprint in perpetuity. It is made available under aCC-BY 4.0 International license.

163 initiated frequently when the junctions were shortening rather than when they were extending
164 (Fig. 2g). Approximately 80% of the large actin protrusions emerged at shortening junctions
165 (Fig. 2h). These observations raise the possibility that junction contraction sensitizes cells to
166 the formation of large protrusions. To evaluate this possibility, we depleted MRLC or Rock,
167 an upstream activator of myosin II[1,5]. Depletion of these factors suppressed the emergence of
168 large protrusions in Pak3 RNAi cells (Fig. 2f). Collectively, these results suggest that Pak3
169 suppresses the formation of branched network-containing actin protrusions at cell–cell
170 junctions upon contraction of the junctions.
171
172 **Pak3 retains myosin II cables and tension at cell–cell junctions.** During the emergence of
173 aberrant actin protrusions, the junctions failed to continue shortening and instead re-extended
174 (Fig. 2g), implying that while large protrusions are induced upon junction contraction, they in
175 turn perturb contraction. To understand how junction contraction is compromised, we
176 examined the dynamics of myosin II. Time-lapse imaging of GFP-tagged MRLC
177 (MRLC::GFP) showed that the majority of MRLC::GFP signals were observed as a single
178 cable at cell–cell junctions (Fig. 3a). In the control cells, the MRLC::GFP signals still remained
179 as a single cable at the initiation of junction shortening; however, when the junction lengths

bioRxiv preprint doi: https://doi.org/10.1101/743237; this version posted August 22, 2019. The copyright holder for this preprint (which was not certified by peer review) is the author/funder, who has granted bioRxiv a license to display the preprint in perpetuity. It is made available under aCC-BY 4.0 International license.

were decreased, the MRLC::GFP signals split into two distinct cables at the shortening junctions (Fig. 3a, arrowheads). In Pak3-depleted cells, we found that the MRLC::GFP cables had already split before the junctions had shortened sufficiently (Fig. 3a, arrowheads). Measurement of the lengths of junctions when MRLC::GFP cables split revealed that depleting Pak3 significantly increased their length from 1.3 ± 0.41 to 2.2 ± 0.72 μm (Fig. 3b). Since E-Cad::GFP signals did not segregate at shortening junctions (Fig. 1d), this observation suggests that myosin II is dissociated from shortening cell–cell junctions.

To examine the interplay between the large actin protrusions and myosin II cables in Pak3 RNAi cells, we next observed myosin II and actin dynamics simultaneously using MRLC::GFP and Lifeact tagged with red fluorescent protein (Lifeact::Ruby)[34]. We categorized the aberrant actin and myosin II dynamics into the following three groups and examined their proportions: splitting of myosin II cables, generation of large actin protrusions, and both (Fig. 3c–e). At junctions greater than 3 μm in length, which roughly exceed the mean + 1 S.D. of the length with split myosin II cables in Pak3-depleted cells (Fig. 3b), large protrusive structures were still generated in the absence of myosin II splitting, suggesting that the dissociation of myosin II from cell–cell junctions is not located upstream from the formation of aberrant actin protrusions (Fig. 3d). In contrast, at junctions less than 3 μm in length (or

bioRxiv preprint doi: https://doi.org/10.1101/743237; this version posted August 22, 2019. The copyright holder for this preprint (which was not certified by peer review) is the author/funder, who has granted bioRxiv a license to display the preprint in perpetuity. It is made available under aCC-BY 4.0 International license.

197 shortening junctions), most of the splitting cables were observed concomitantly with large actin
198 protrusions (Fig. 3e). This observation raises the possibility that the emergence of large actin
199 protrusions triggers the segregation of myosin II at shortening junctions. To test this possibility,
200 we depleted Abi in Pak3 RNAi cells. This manipulation reduced the length at which the
201 junctions showed split myosin II cables, suggesting that myosin II dissociation is associated
202 with the generation of aberrant actin protrusions (Fig. 3f,g).

203 We hypothesized that the failure of junction contraction observed in Pak3-depleted
204 cells was attributed to the dissociation of myosin II from shortening junctions and the
205 consequent reduction in tension at the junctions. To evaluate tension at junctions, we cut the
206 junctions by ablation with a 365-nm laser and measured the displacement of their vertices,
207 which reflects junctional tension (Fig. 3h,i)[39,40]. This showed that the initial speed of
208 displacement upon laser ablation was decreased in Pak3 RNAi cells (Fig. 3i). Collectively,
209 these results suggest that Pak3 ensures junction contraction by retaining myosin II attachment
210 and tension at cell–cell junctions.

211

212 **Dilution of E-cadherin at cell–cell junctions mediates myosin II dissociation.** To clarify
213 how the large actin protrusions and consequent segregation of myosin II at shortening junctions

bioRxiv preprint doi: https://doi.org/10.1101/743237; this version posted August 22, 2019. The copyright holder for this preprint (which was not certified by peer review) is the author/funder, who has granted bioRxiv a license to display the preprint in perpetuity. It is made available under aCC-BY 4.0 International license.

214 are connected, we again explored the distribution of E-cadherin, since it is a central component
215 of the cadherin–catenin core complex that acts as a scaffold for actomyosin at AJs[29,41].
216 Magnified time-lapse images of E-Cad::GFP in the control cells revealed that while the
217 majority of E-Cad::GFP signals were localized along cell–cell junctions, they frequently
218 formed small protrusions arising from the junctions (Fig. 4a, arrowheads; Supplementary
219 Movie 5). These protrusions were positive for E-Cad::GFP and Lifeact::Ruby, suggesting that
220 E-cadherin is associated with actin protrusions (Fig. 4b). We also found that E-Cad::GFP levels
221 were sometimes decreased locally at the base of these protrusions on the junctions (Fig. 4a,
222 broken line). These observations suggest that actin protrusions can reduce the local levels of
223 junctional E-cadherin. The junctions in Pak3-depleted cells also generated E-Cad::GFP-
224 positive protrusions, but they were larger in size (Fig. 4a, arrowheads; Supplementary Movie
225 6). In addition, the local regions associated with E-Cad::GFP dilution on junctions were
226 extended (Fig. 4a, broken lines). These observations suggest that Pak3 depletion enhances the
227 reduction in E-cadherin levels at cell–cell junctions.

228 We then asked whether this dilution of E-cadherin is involved in the formation of
229 aberrant actin protrusions and/or myosin II segregation. To this end, we upregulated E-cadherin
230 levels in the Pak3-depleted A8a cells and examined if this manipulation suppressed these

bioRxiv preprint doi: https://doi.org/10.1101/743237; this version posted August 22, 2019. The copyright holder for this preprint (which was not certified by peer review) is the author/funder, who has granted bioRxiv a license to display the preprint in perpetuity. It is made available under aCC-BY 4.0 International license.

231 dynamics. A comparison of E-Cad::GFP intensities at the local regions with and without actin
232 protrusions ($Int_{w/}$ and $Int_{w/o}$, respectively) within each junction in Pak3-depleted cells revealed
233 that the levels of endogenous E-cadherin tagged with GFP (knock-in, KI) were significantly
234 reduced to approximately 80% in the presence of actin protrusions (Fig. 4c–e). Overexpressing
235 E-Cad::GFP under the control of the ubiquitin promoter, which slightly increased E-cadherin
236 protein levels[42], attenuated the local reduction in E-Cad::GFP levels upon the formation of
237 actin protrusions (Fig. 4c,e). However, this manipulation did not attenuate the generation of
238 large actin protrusions, indicating that E-cadherin dilution is located downstream from the
239 formation of actin protrusions (Fig. 4f).

240 We next induced the overexpression of intact E-cadherin[43]. This manipulation
241 suppressed the dissociation of myosin II from cell–cell junctions in Pak3 RNAi cells, which
242 was indicated by a reduction in the length of junctions with split MRLC::GFP cables, similar
243 to the effect of Abi RNAi (Figs. 3f,g and 4g,h). Taken together, these results suggest that the
244 dilution of E-cadherin at cell–cell junctions induced by actin protrusions results in the inability
245 of Pak3-depleted cells to retain myosin II at the junctions.

246

247 **E-cadherin maintains tissue dynamics.** We finally explored whether overexpressing E-

bioRxiv preprint doi: https://doi.org/10.1101/743237; this version posted August 22, 2019. The copyright holder for this preprint (which was not certified by peer review) is the author/funder, who has granted bioRxiv a license to display the preprint in perpetuity. It is made available under aCC-BY 4.0 International license.

248 cadherin also restored tissue dynamics in Pak3 RNAi flies. E-Cad::GFP overexpression
249 partially restored the junction-remodeling frequency in Pak3-depleted cells and slightly
250 decreased the frequency of the shortening defect (Fig. 5a). In addition, this manipulation
251 decreased the number of adult males with abnormal orientations of genitalia (Figs. 1b and 5b).
252 These results suggest that the E-cadherin-mediated association of myosin II at junctions is
253 required for completing junction shortening, leading to proper cell intercalation and epithelial
254 cell movement.
255
256 **Discussion**
257 During cell–cell junction shortening, actin and myosin II accumulate at junctions, and the
258 resultant actomyosin bundles generate contractile forces[5,44]. In contrast, previous reports
259 demonstrated that myosin II contractility potentiates actin unbundling and depolymerization in
260 vitro and in vivo[45,46], which could compromise contraction. It has also been recently shown
261 that cell–cell contacts concomitantly induce both myosin II-driven contraction and protrusive
262 branched actin-mediated extension[10]. Therefore, it would be reasonable to suppose that there
263 is a mechanism to maintain contractility for persistent cell–cell junction shortening. In this
264 study, we found that, in the absence of Pak3, aberrant actin dynamics at junctions disturb

bioRxiv preprint doi: https://doi.org/10.1101/743237; this version posted August 22, 2019. The copyright holder for this preprint (which was not certified by peer review) is the author/funder, who has granted bioRxiv a license to display the preprint in perpetuity. It is made available under aCC-BY 4.0 International license.

junction contraction during their shortening. On the basis of our results, we suppose the following scenario in cells lacking Pak3 (Fig. 5c): (i) upon contraction of cell–cell junctions, actin dynamics at the junctions are altered to generate abnormally large protrusions; (ii) these aberrant protrusions cause the dilution of E-cadherin at the junctions; (iii) the decrease in E-cadherin levels weakens the association of myosin II cables at the junctions; and (iv) the dissociation of myosin II cables causes insufficient transmission of their contractility to the junctions, leading to a decrease in junctional tension and incomplete junction shortening. In the normal condition (in the presence of Pak3), Pak3 blocks excess formation of actin protrusions, keeps E-cadherin and myosin II localized at junctions, and thus ensures persistent junction contraction, which is necessary for completing cell–cell junction remodeling and the resultant tissue movement (Fig. 5c).

This scenario proposes a possible negative feedback mechanism (Fig. 5c, green arrows); the contractile forces of myosin II at junctions drive junction shortening, but they can oppositely perturb shortening by concomitantly altering actin dynamics, such as inducing the formation of WRC-dependent branched actin networks. Since Pak proteins are reported to regulate actin dynamics[47,48], Pak3 is a candidate for counteracting such undesirable actin dynamics, although its precise molecular mechanism is still unclear. Considering that Pak

bioRxiv preprint doi: https://doi.org/10.1101/743237; this version posted August 22, 2019. The copyright holder for this preprint (which was not certified by peer review) is the author/funder, who has granted bioRxiv a license to display the preprint in perpetuity. It is made available under aCC-BY 4.0 International license.

282 proteins and the WRC are activated by Rho GTPases[47,49,50], it is possible that the presence of
283 Pak3 sequesters these GTPases from the branching network-forming machineries. In addition,
284 since Pak proteins are involved in a diverse array of biological events and have various
285 substrates[31,51–54], the identification of Pak3 substrates in this context will further deepen our
286 understanding of how cells accomplish persistent junctional dynamics.
287
288 **Methods**
289 **Fly genetics.** The following *Drosophila* stocks were used: w^{1118}, *hs-flp*, *Act>CD2>Gal4*, *UAS-*
290 *mCD8::mCherry*, *UAS-Lifeact::GFP*, *UAS-Lifeact::Ruby*, *His2Av::mRFP*, *UAS-Dicer2*, *UAS-*
291 *MRLC* (*sqh*) *RNAi* (JF01103), and *UAS-Abi RNAi* (HMC03190) (Bloomington Drosophila
292 Stock Center); *UAS-MRLC RNAi* (7916) and *UAS-Rock RNAi* (3793) (Vienna Drosophila
293 Resource Center); *UAS-Pak3 RNAi* (14895R-1) (National Institute of Genetics, Japan); *UAS-*
294 *E-cadherin* and *Ubi-E-cadherin::GFP* (Drosophila Genomics and Genetic Resources); *UAS-*
295 *Pak3::GFP* (a gift from S. Hayashi); $AbdB\text{-}Gal4^{LDN}$ (ref. 24); $Pak3^{d02472}$ (ref. 30); *E-*
296 *Cad::GFP*[28]; sqh^{AX3}*;sqh-sqh::GFP* (MRLC::GFP)[55]; *sqh-UtrABD::GFP*[36]; and *UAS-*
297 *Histone2B (H2B)::ECFP*[56]. The flies were raised, and all experiments were performed at 25°C.
298 Somatic RNAi clones were induced using the FLP/FRT technique[57] in white pupae (at 0 h

bioRxiv preprint doi: https://doi.org/10.1101/743237; this version posted August 22, 2019. The copyright holder for this preprint (which was not certified by peer review) is the author/funder, who has granted bioRxiv a license to display the preprint in perpetuity. It is made available under aCC-BY 4.0 International license.

299 APF) by heat shock (37°C for 15 min).

300 **Antibodies.** Antibodies against Dlg (4F3; Developmental Studies Hybridoma Bank) and

301 Pak3[58] were used.

302 **Immunohistochemistry.** Pupae were dissected and fixed in 4% paraformaldehyde in

303 phosphate-buffered saline (PBS) for 20 min at room temperature (RT) and permeabilized with

304 0.1% Triton X-100 in PBS (PBT). The permeabilized samples were incubated in PBT with 5%

305 donkey serum (blocking buffer) for 30 min at RT, incubated with primary antibodies in

306 blocking buffer overnight at 4°C, washed with PBT, incubated in blocking buffer for 30 min

307 at RT, and incubated with secondary antibodies (Alexa Fluor 647 goat anti-mouse IgG; Life

308 Technologies) in blocking buffer for 2 h at RT. The samples were washed with PBT and

309 mounted with 70% glycerol in PBS. Fluorescence microscopy images were captured on a TCS

310 SP8 with a 63× numerical aperture (NA) 1.3 glycerol objective (Leica). Images are maximum

311 intensity projections of serial optical sections taken at a 0.5-μm z step size.

312 **Live imaging.** Pupae were prepared as described previously[21]. Time-lapse imaging of flies was

313 performed using an SP8 confocal microscope with 63× NA 1.3 glycerol and 20× NA 0.75 dry

314 objectives (Leica), except for the images in Figs. 1D and 3A and Movies S1 and S2, which

315 were obtained using an inverted microscope with a 60× NA 1.3 silicone oil objective

bioRxiv preprint doi: https://doi.org/10.1101/743237; this version posted August 22, 2019. The copyright holder for this preprint (which was not certified by peer review) is the author/funder, who has granted bioRxiv a license to display the preprint in perpetuity. It is made available under aCC-BY 4.0 International license.

316 (Olympus) equipped with a spinning-disc confocal unit (CSU-W1; Yokogawa) and a Zyla 4.2
317 PLUS sCMOS camera (Andor). All images are maximum intensity projections at the level of
318 the AJs taken at a 1-μm z step size, except for images showing rotation of the genitalia (Fig.
319 1A), which are maximum intensity projections of the posterior end of flies taken at a 5-μm z
320 step size. Time-lapse images were acquired at 10-s, 20-s, 2-min, or 10-min intervals.

321 **Laser ablation.** Laser ablation was performed with a 365-nm MicroPoint laser (Andor). To
322 cut junctions, a 365-nm laser pulse was applied for 1 iteration to the point at the middle of the
323 targeted junctions at the level of AJs, which was determined by maximum E-Cad::GFP
324 intensity.

325 **Tracking of junction dynamics.** Junction dynamics were analyzed manually with Fiji
326 software. Projected time-lapse images were used. In the A8a epithelia, junctions were tracked
327 from the initiation of movement (26 h APF) to the time when the genitalia angles were greater
328 than 90° (30 h APF)[21]. Junctions that were remodeled at least once were categorized as
329 "remodeling." Junctions that failed to resolve four-way vertices were categorized as "growth
330 defect." Junctions that remodeled, but then immediately retracted the new junctions and re-
331 formed in the original direction were also categorized as "growth defect." Junctions that
332 shortened to less than 1.5 μm in length, but failed to form four-way vertices were categorized

bioRxiv preprint doi: https://doi.org/10.1101/743237; this version posted August 22, 2019. The copyright holder for this preprint (which was not certified by peer review) is the author/funder, who has granted bioRxiv a license to display the preprint in perpetuity. It is made available under aCC-BY 4.0 International license.

as "shortening defect." "No remodeling" included junctions that did not shorten to less than 1.5 μm in length.

Quantification of junction length, fluorescence intensity, and actin dynamics. Cell–cell junction length was determined as the distance between vertices, except for when split MRLC::GFP cables emerged, which was determined as the distance between myosin II cables in cells surrounding the shortening junctions when the myosin II cables in cells forming the shortening junctions first segregated. The mean fluorescence intensity of E-Cad::GFP at a region on the junctions was measured using a line along the junctions. The frequency of the emergence of large actin protrusions was counted at each junction within 1 h.

Statistical analysis. All statistical analyses were performed using R. To assess significance, the following tests were used: two-way analysis of variance (ANOVA) followed by Tukey's test for comparing the percentage of remodeling junctions; two-way ANOVA followed by Dunnett's test for comparing junction length with split myosin II cables among Pak3 RNAi cells; unpaired two-tailed *t*-test for comparing two samples; one-sample *t*-test for the significance of the $Int_{w/}/Int_{w/o}$ ratio with test values of 1; and unpaired two-tailed Mann-Whitney *U*-test followed by Bonferroni's test for comparing the frequency of the appearance of actin diffusive structures.

bioRxiv preprint doi: https://doi.org/10.1101/743237; this version posted August 22, 2019. The copyright holder for this preprint (which was not certified by peer review) is the author/funder, who has granted bioRxiv a license to display the preprint in perpetuity. It is made available under aCC-BY 4.0 International license.

350

351 **Acknowledgements**

352 We thank S. Hayashi for providing the *UAS-Pak3::GFP* fly strain; N.T. Sherwood for
353 providing the *Pak3*^{d02472} fly strain; T. Lecuit for providing the *sqh-UtrABD::GFP* fly strain; N.
354 Harden for providing the anti-Pak3 antibodies; E. Maekawa, A. Isomura and Y. Umegaki, S.
355 Sato, K. Takahashi and A. Kuranaga for supporting the experiments; and members of the S.
356 Hayashi, T. Nishimura, S. K. Yoo, Y.-C. Wang, and all member of our laboratory for
357 discussions. We are grateful to "ThinkSCIENCE" for language proofreading of the manuscript.
358 This work was supported by grants from JST CREST Grant Number JPMJCR1852, Japan
359 (E.K.), the research grand for Astellas Foundation for Research on Metabolic Disorders (E.K.),
360 the Takeda Science Foundation (E.K.), the Japan Foundation for Applied Enzymology (E.K.),
361 MEXT KAKENHI grant number JP26114003 (E.K.), and JSPS KAKENHI grant numbers
362 JP24687027 (E.K.), JP16H04800 (E.K.), and JP18K14691 (H.U).

363

364

365 **Author contributions**

366 H.U. conceived the study, performed the experiments, analyzed the data, and wrote the

bioRxiv preprint doi: https://doi.org/10.1101/743237; this version posted August 22, 2019. The copyright holder for this preprint (which was not certified by peer review) is the author/funder, who has granted bioRxiv a license to display the preprint in perpetuity. It is made available under aCC-BY 4.0 International license.

manuscript. E.K. conceived the study, analyzed the data, and revised the manuscript.

Competing interests

The authors declare no competing interests.

Materials and correspondence

Further information and requests for resources and reagents should be directed to and will be fulfilled by the corresponding author, Erina Kuranaga (erina.kuranaga.d1@tohoku.ac.jp).

REFERENCES

1. Lecuit, T., Lenne, P.-F. & Munro, E. Force Generation, Transmission, and Integration during Cell and Tissue Morphogenesis. *Annu. Rev. Cell Dev. Biol.* (2011). doi:10.1146/annurev-cellbio-100109-104027

2. Murrell, M., Oakes, P. W., Lenz, M. & Gardel, M. L. Forcing cells into shape: The mechanics of actomyosin contractility. *Nature Reviews Molecular Cell Biology* (2015). doi:10.1038/nrm4012

3. Krause, M. & Gautreau, A. Steering cell migration: Lamellipodium dynamics and the

bioRxiv preprint doi: https://doi.org/10.1101/743237; this version posted August 22, 2019. The copyright holder for this preprint (which was not certified by peer review) is the author/funder, who has granted bioRxiv a license to display the preprint in perpetuity. It is made available under aCC-BY 4.0 International license.

regulation of directional persistence. *Nature Reviews Molecular Cell Biology* (2014). doi:10.1038/nrm3861

4. Heisenberg, C.-P. & Bellaïche, Y. Forces in Tissue Morphogenesis and Patterning. *Cell* **153**, 948–962 (2013).

5. Levayer, R. & Lecuit, T. Biomechanical regulation of contractility: Spatial control and dynamics. *Trends in Cell Biology* **22**, 61–81 (2012).

6. Huse, M. Mechanical forces in the immune system. *Nat. Rev. Immunol.* **17**, 679–690 (2017).

7. Pinheiro, D. & Bellaïche, Y. Mechanical Force-Driven Adherens Junction Remodeling and Epithelial Dynamics. *Dev. Cell* **47**, 3–19 (2018).

8. Mayor, R. & Etienne-Manneville, S. The front and rear of collective cell migration. *Nat. Rev. Mol. Cell Biol.* **17**, 97–109 (2016).

9. Ladoux, B., Mège, R. M. & Trepat, X. Front-Rear Polarization by Mechanical Cues: From Single Cells to Tissues. *Trends in Cell Biology* (2016). doi:10.1016/j.tcb.2016.02.002

10. Del Signore, S. J., Cilla, R. & Hatini, V. The WAVE Regulatory Complex and Branched F-Actin Counterbalance Contractile Force to Control Cell Shape and

bioRxiv preprint doi: https://doi.org/10.1101/743237; this version posted August 22, 2019. The copyright holder for this preprint (which was not certified by peer review) is the author/funder, who has granted bioRxiv a license to display the preprint in perpetuity. It is made available under aCC-BY 4.0 International license.

Packing in the Drosophila Eye. *Dev. Cell* **44**, 471-483.e4 (2018).

11. Walck-Shannon, E. & Hardin, J. Cell intercalation from top to bottom. *Nat. Rev. Mol. Cell Biol.* **15**, 34–48 (2014).

12. Guillot, C. & Lecuit, T. Mechanics of epithelial tissue homeostasis and morphogenesis. *Science* **340**, 1185–1189 (2013).

13. Irvine, K. D. & Wieschaus, E. Cell intercalation suring Drosophila germband extension and its regulaton by pair00rule segmentation genes. *Development* **120**, 827–841 (1994).

14. Guirao, B. & Bellaïche, Y. Biomechanics of cell rearrangements in Drosophila. *Current Opinion in Cell Biology* **48**, 113–124 (2017).

15. Bertet, C., Sulak, L. & Lecuit, T. Myosin-dependent junction remodelling controls planar cell intercalation and axis elongation. *Nature* **429**, 667–71 (2004).

16. Martin, A. C. Pulsation and stabilization: Contractile forces that underlie morphogenesis. *Developmental Biology* (2010). doi:10.1016/j.ydbio.2009.10.031

17. Fernandez-Gonzalez, R., Simoes, S. de M., Röper, J.-C., Eaton, S. & Zallen, J. A. Myosin II Dynamics Are Regulated by Tension in Intercalating Cells. *Dev. Cell* **17**, 736–743 (2009).

bioRxiv preprint doi: https://doi.org/10.1101/743237; this version posted August 22, 2019. The copyright holder for this preprint (which was not certified by peer review) is the author/funder, who has granted bioRxiv a license to display the preprint in perpetuity. It is made available under aCC-BY 4.0 International license.

418 18. Simões, S. de M. *et al.* Rho-Kinase Directs Bazooka/Par-3 Planar Polarity during
419 Drosophila Axis Elongation. *Dev. Cell* **19**, 377–388 (2010).
420 19. Zallen, J. A. & Wieschaus, E. Patterned Gene Expression Directs Bipolar Planar
421 Polarity in Drosophila. *Dev. Cell* **6**, 343–355 (2004).
422 20. Sato, K. *et al.* Left–right asymmetric cell intercalation drives directional collective cell
423 movement in epithelial morphogenesis. *Nat. Commun.* **6**, 10074 (2015).
424 21. Kuranaga, E. *et al.* Apoptosis controls the speed of looping morphogenesis in
425 Drosophila male terminalia. *Development* **138**, 1493–1499 (2011).
426 22. Suzanne, M. *et al.* Coupling of apoptosis and L/R patterning controls stepwise organ
427 looping. *Curr. Biol.* **20**, 1773–1778 (2010).
428 23. Sato, K., Hiraiwa, T. & Shibata, T. Cell Chirality Induces Collective Cell Migration in
429 Epithelial Sheets. *Phys. Rev. Lett.* **115**, (2015).
430 24. de Navas, L., Foronda, D., Suzanne, M. & Sánchez-Herrero, E. A simple and efficient
431 method to identify replacements of P-lacZ by P-Gal4 lines allows obtaining Gal4
432 insertions in the bithorax complex of Drosophila. *Mech. Dev.* **123**, 860–867 (2006).
433 25. Brand, A. H. & Perrimon, N. Targeted gene expression as a means of altering cell fates
434 and generating dominant phenotypes. *Development* **118**, 401–415 (1993).

bioRxiv preprint doi: https://doi.org/10.1101/743237; this version posted August 22, 2019. The copyright holder for this preprint (which was not certified by peer review) is the author/funder, who has granted bioRxiv a license to display the preprint in perpetuity. It is made available under aCC-BY 4.0 International license.

435 26. Dietzl, G. *et al.* A genome-wide transgenic RNAi library for conditional gene
436 inactivation in Drosophila. *Nature* **448**, 151–156 (2007).
437 27. Macara, I. G. Parsing the polarity code. *Nature Reviews Molecular Cell Biology*
438 (2004). doi:10.1038/nrm1332
439 28. Huang, J., Zhou, W., Dong, W., Watson, A. M. & Hong, Y. From the Cover: Directed,
440 efficient, and versatile modifications of the Drosophila genome by genomic
441 engineering. *Proc. Natl. Acad. Sci. U. S. A.* **106**, 8284–9 (2009).
442 29. Takeichi, M. Dynamic contacts: Rearranging adherens junctions to drive epithelial
443 remodelling. *Nature Reviews Molecular Cell Biology* **15**, 397–410 (2014).
444 30. Ozdowski, E. F., Gayle, S., Bao, H., Zhang, B. & Sherwood, N. T. Loss of Drosophila
445 melanogaster p21-activated kinase 3 suppresses defects in synapse structure and
446 function caused by spastin mutations. *Genetics* (2011).
447 doi:10.1534/genetics.111.130831
448 31. Bokoch, G. M. Biology of the p21-Activated Kinases. *Annu. Rev. Biochem.* (2003).
449 doi:10.1146/annurev.biochem.72.121801.161742
450 32. Hofmann, C. The genetics of Pak. *J. Cell Sci.* (2004). doi:10.1242/jcs.01392
451 33. Mentzel, B. & Raabe, T. Phylogenetic and structural analysis of the Drosophila

bioRxiv preprint doi: https://doi.org/10.1101/743237; this version posted August 22, 2019. The copyright holder for this preprint (which was not certified by peer review) is the author/funder, who has granted bioRxiv a license to display the preprint in perpetuity. It is made available under aCC-BY 4.0 International license.

melanogaster p21-activated kinase DmPAK3. *Gene* (2005). doi:10.1016/j.gene.2004.12.030

34. Riedl, J. *et al.* Lifeact: A versatile marker to visualize F-actin. *Nat. Methods* (2008). doi:10.1038/nmeth.1220

35. Burkel, B. M., Von Dassow, G. & Bement, W. M. Versatile fluorescent probes for actin filaments based on the actin-binding domain of utrophin. *Cell Motil. Cytoskeleton* (2007). doi:10.1002/cm.20226

36. Rauzi, M., Lenne, P.-F. & Lecuit, T. Planar polarized actomyosin contractile flows control epithelial junction remodelling. *Nature* **468**, 1110–1114 (2010).

37. Eden, S., Rohatgi, R., Podtelejnikov, A. V., Mann, M. & Kirschner, M. W. Mechanism of regulation of WAVE1-induced actin nucleation by Rac1 and Nck. *Nature* (2002). doi:10.1038/nature00859

38. Chen, B. *et al.* The WAVE regulatory complex links diverse receptors to the actin cytoskeleton. *Cell* **156**, 195–207 (2014).

39. Rauzi, M., Verant, P., Lecuit, T. & Lenne, P.-F. Nature and anisotropy of cortical forces orienting Drosophila tissue morphogenesis. *Nat. Cell Biol.* **10**, 1401–1410 (2008).

bioRxiv preprint doi: https://doi.org/10.1101/743237; this version posted August 22, 2019. The copyright holder for this preprint (which was not certified by peer review) is the author/funder, who has granted bioRxiv a license to display the preprint in perpetuity. It is made available under aCC-BY 4.0 International license.

469 40. Umetsu, D. *et al.* Local Increases in Mechanical Tension Shape Compartment

470 Boundaries by Biasing Cell Intercalations. *Curr. Biol.* **24**, 1798–1805 (2014).

471 41. Lecuit, T. & Yap, A. S. E-cadherin junctions as active mechanical integrators in tissue

472 dynamics. *Nature Cell Biology* **17**, 533–539 (2015).

473 42. Oda, H. & Tsukita, S. Real-time imaging of cell-cell adherens junctions reveals that

474 Drosophila mesoderm invagination begins with two phases of apical constriction of

475 cells. *J. Cell Sci.* **114**, 493–501 (2001).

476 43. Oda, H. & Tsukita, S. Nonchordate Classic Cadherins Have a Structurally and

477 Functionally Unique Domain That Is Absent from Chordate Classic Cadherins. *Dev.*

478 *Biol.* **216**, 406–422 (1999).

479 44. Martin, A. C. & Goldstein, B. Apical constriction: themes and variations on a cellular

480 mechanism driving morphogenesis. *Development* (2014). doi:10.1242/dev.102228

481 45. Medeiros, N. A., Burnette, D. T. & Forscher, P. Myosin II functions in actin-bundle

482 turnover in neuronal growth cones. *Nat. Cell Biol.* (2006). doi:10.1038/ncb1367

483 46. Haviv, L., Gillo, D., Backouche, F. & Bernheim-Groswasser, A. A Cytoskeletal

484 Demolition Worker: Myosin II Acts as an Actin Depolymerization Agent. *J. Mol. Biol.*

485 (2008). doi:10.1016/j.jmb.2007.09.066

bioRxiv preprint doi: https://doi.org/10.1101/743237; this version posted August 22, 2019. The copyright holder for this preprint (which was not certified by peer review) is the author/funder, who has granted bioRxiv a license to display the preprint in perpetuity. It is made available under aCC-BY 4.0 International license.

47. Ridley, A. J. Rho GTPases and actin dynamics in membrane protrusions and vesicle trafficking. *Trends in Cell Biology* (2006). doi:10.1016/j.tcb.2006.08.006

48. Dráber, P., Sulimenko, V. & Dráberová, E. Cytoskeleton in mast cell signaling. *Frontiers in Immunology* (2012). doi:10.3389/fimmu.2012.00130

49. Heasman, S. J. & Ridley, A. J. Mammalian Rho GTPases: new insights into their functions from in vivo studies. *Nat. Rev. Mol. Cell Biol.* **9**, 690–701 (2008).

50. Ridley, A. J. Rho GTPases and cell migration. *J. Cell Sci.* (2001).

51. Radu, M., Semenova, G., Kosoff, R. & Chernoff, J. PAK signalling during the development and progression of cancer. *Nature Reviews Cancer* (2014). doi:10.1038/nrc3645

52. Duan, R. *et al.* Group I PAKs function downstream of Rac to promote podosome invasion during myoblast fusion in vivo. *J. Cell Biol.* (2012). doi:10.1083/jcb.201204065

53. Kamiyama, D. *et al.* Specification of Dendritogenesis Site in Drosophila aCC Motoneuron by Membrane Enrichment of Pak1 through Dscam1. *Dev. Cell* (2015). doi:10.1016/j.devcel.2015.09.007

54. Chiang, Y. -t. A. & Jin, T. p21-Activated protein kinases and their emerging roles in

bioRxiv preprint doi: https://doi.org/10.1101/743237; this version posted August 22, 2019. The copyright holder for this preprint (which was not certified by peer review) is the author/funder, who has granted bioRxiv a license to display the preprint in perpetuity. It is made available under aCC-BY 4.0 International license.

glucose homeostasis. *AJP Endocrinol. Metab.* (2014).

doi:10.1152/ajpendo.00506.2013

55. Royou, A., Sullivan, W. & Karess, R. Cortical recruitment of nonmuscle myosin II in early syncytial Drosophila embryos: Its role in nuclear axial expansion and its regulation by Cdc2 activity. *J. Cell Biol.* **158**, 127–137 (2002).

56. Koto, A., Kuranaga, E. & Miura, M. Temporal regulation of Drosophila IAP1 determines caspase functions in sensory organ development. *J. Cell Biol.* **187**, 219–231 (2009).

57. Xu, T. & Rubin, G. M. Analysis of genetic mosaics in developing and adult Drosophila tissues. *Development* **117**, 1223–1237 (1993).

58. Bahri, S. *et al.* The leading edge during dorsal closure as a model for epithelial plasticity: Pak is required for recruitment of the Scribble complex and septate junction formation. *Development* (2010). doi:10.1242/dev.045088

Figure Legends

Figure 1 | Pak3 is required for cell–cell junction shortening during epithelial junction

bioRxiv preprint doi: https://doi.org/10.1101/743237; this version posted August 22, 2019. The copyright holder for this preprint (which was not certified by peer review) is the author/funder, who has granted bioRxiv a license to display the preprint in perpetuity. It is made available under aCC-BY 4.0 International license.

520 **remodeling.** (**a**) Representative time-lapse images of male genitalia observed from the
521 posterior end during rotation. The ventral side is located at the top. Nuclei in the A8a cells and
522 the whole body are depicted in green and purple, respectively. Yellow and white arrows
523 indicate the movements of genitalia and the A8a epithelia, respectively. Scale bar, 100 μm. (**b**)
524 Left, schema for the categorization of genitalia angles. Yellow arrow indicates genitalia
525 movement. Gray indicates the 360° rotation of genitalia (normal orientation). Right,
526 percentages of male adult flies with the indicated genitalia angles are shown. Parentheses
527 indicate the number of males examined. (**c**) A8a epithelia at 28 h APF immunostained for Pak3
528 and Dlg. Pak3 RNAi cells are indicated with mCherry signals. Scale bar, 10 μm. Broken lines
529 indicate the edges of Pak3 RNAi clones. (**d**) Representative time-lapse images of E-Cad::GFP
530 at remodeling junctions. Stars and triangles indicate cells forming the shortening junctions.
531 Orange, blue, and green arrowheads indicate shortening junctions, four-way vertices, and
532 growing junctions, respectively. Scale bar, 5 μm. (**e**) Schema representing the categorization
533 of junction dynamics. (**f**) Mean ± S.D. of the percentages of junctions with the categorized
534 dynamics. Bar colors correspond to (e). Parentheses indicate the number of examined junctions
535 from 3 pupae per genotype. *P*-values by Tukey's test. Genotypes: (**a**)
536 *+/Y;His2Av::mRFP/+;AbdB-Gal4, UAS-H2B::ECFP/+* (Control) and

bioRxiv preprint doi: https://doi.org/10.1101/743237; this version posted August 22, 2019. The copyright holder for this preprint (which was not certified by peer review) is the author/funder, who has granted bioRxiv a license to display the preprint in perpetuity. It is made available under aCC-BY 4.0 International license.

537 *+/Y;His2Av::mRFP/+;AbdB-Gal4, UAS-H2B::ECFP/UAS-Pak3 RNAi*; (**b**) *+/Y;;AbdB-*

538 *Gal4/+* (Control), *+/Y;;AbdB-Gal4/UAS-MRLC RNAi*, *+/Y;;AbdB-Gal4/UAS-Pak3 RNAi*,

539 *+/Y;UAS-Dicer2/+;AbdB-Gal4/UAS-Pak3 RNAi*, and *+/Y;;AbdB-Gal4, UAS-*

540 *Pak3::GFP/UAS-Pak3 RNAi*; (**c**) *hs-flp/Y;E-Cad::GFP;Act>CD2>Gal4, UAS-*

541 *mCD8::mCherry/UAS-Pak3 RNAi*; (**d** and **f**) *+/Y;E-Cad::GFP;AbdB-Gal4, UAS-*

542 *H2B::ECFP/+* (Control), *+/Y;E-Cad::GFP;AbdB-Gal4, UAS-H2B::ECFP/UAS-Pak3 RNAi,*

543 and *+/Y;E-Cad::GFP;Pak3*^{d02472}.

544 **Figure 2 | Pak3 depletion enhances the formation of large actin protrusions.** (**a**) Images of

545 actin labeled with Lifeact::GFP in the A8a cells. Arrowheads indicate some actin protrusions.

546 Scale bar, 10 μm. (**b**) Magnified time-lapse images of Lifeact::GFP at cell–cell junctions. Scale

547 bar, 3 μm. (**c**) Mean ± S.D. of the width and height of actin protrusion. Parentheses indicate

548 the number of examined protrusions from 5 pupae per genotype. *P*-values by unpaired *t*-test.

549 (**d**) Images of actin labeled with UtrABD::GFP in the A8a cells. Arrowheads indicate some

550 actin protrusions. Scale bar, 10 μm. (**e**) Schema of large actin (magenta) protrusions at a

551 boundary (black). (**f**) Percentages of junctions generating large actin protrusions for the

552 indicated number of times per hour are shown. Parentheses indicate the number of examined

553 junctions from 4–5 pupae per genotype. *P*-values by Mann-Whitney *U*-test. (**g**) Graph showing

bioRxiv preprint doi: https://doi.org/10.1101/743237; this version posted August 22, 2019. The copyright holder for this preprint (which was not certified by peer review) is the author/funder, who has granted bioRxiv a license to display the preprint in perpetuity. It is made available under aCC-BY 4.0 International license.

554 the length of a representative junction that repeats shortening and re-extension. The timings
555 when large actin protrusions emerge are shown in magenta. (**h**) Mean ± S.D. of the timing of
556 the onset of large actin protrusion formation. Parenthesis indicates the number of protrusions
557 from 15 junctions of 3 pupae. Genotypes: (**a**–**c**) *+/Y;UAS-Lifeact::GFP/+;AbdB-Gal4/+*
558 (Control) and *+/Y;UAS-Lifeact::GFP/+;AbdB-Gal4/UAS-Pak3 RNAi*; (**d**) *+/Y;sqh-*
559 *UtrABD::GFP/+* (Control) and *+/Y;sqh-UtrABD::GFP/+;Pak3^{d02472}*; (**f**) *+/Y;UAS-*
560 *Lifeact::GFP/+;AbdB-Gal4/+* (Control), *+/Y;UAS-Lifeact::GFP/+;AbdB-Gal4/UAS-Pak3*
561 *RNAi*, *+/Y;UAS-Lifeact::GFP/+;AbdB-Gal4, UAS-Pak3::GFP/UAS-Pak3 RNAi*, *+/Y;UAS-*
562 *Lifeact::GFP/UAS-Abi RNAi;AbdB-Gal4/UAS-Pak3 RNAi*, *+/Y;UAS-Lifeact::GFP/UAS-*
563 *MRLC RNAi;AbdB-Gal4/UAS-Pak3 RNAi*, and *+/Y;UAS-Lifeact::GFP/UAS-Rock*
564 *RNAi;AbdB-Gal4/UAS-Pak3 RNAi*; (**g** and **h**) *+/Y;UAS-Lifeact::GFP/+;AbdB-Gal4/UAS-*
565 *Pak3 RNAi*.

566 **Figure 3 | Pak3 depletion causes the dissociation of myosin II and reduces tension at**
567 **junctions.** (**a**) Time-lapse images of MRLC::GFP at shortening junctions. Stars and triangles
568 indicate cells forming the shortening junctions. Orange arrowheads indicate splitting myosin
569 II cables. Scale bar, 3 μm. (**b**) Mean ± S.D. of the lengths of junctions with split myosin II
570 cables; 30 junctions from 3 (Control) and 4 (Pak3 RNAi) pupae were examined. *P*-value by

bioRxiv preprint doi: https://doi.org/10.1101/743237; this version posted August 22, 2019. The copyright holder for this preprint (which was not certified by peer review) is the author/funder, who has granted bioRxiv a license to display the preprint in perpetuity. It is made available under aCC-BY 4.0 International license.

571 unpaired *t*-test. (**c**) Representative images of cell–cell junctions with split myosin II cables,
572 large actin protrusions, and both (from the left). Scale bar, 5 μm. (**d** and **e**) Mean ± S.D. of the
573 percentages of aberrant actin and myosin II dynamics as categorized in (c) at cell–cell junctions
574 larger than (d) and smaller than (e) 3 μm. Parentheses indicate the number of examined
575 junctions from 3 pupae. (**f**) Representative images of split MRLC::GFP cables (orange
576 arrowheads) at junctions. Scale bar, 5 μm. (**g**) Mean ± S.D. of the lengths of junctions with
577 split myosin II cables. Parentheses indicate the number of examined junctions from 5 (Pak3
578 RNAi) and 6 (Pak3 and Abi RNAis) pupae. *P*-value by Dunnett's test. (**h**) Kymographs of cell–
579 cell junctions labeled with E-Cad::GFP and ablated with a 365-nm laser at $t = 0$. (**i**) Mean ±
580 S.D. of the initial speed of vertex displacement after ablation; 32 junctions from 9 (Control)
581 and 8 (Pak3 RNAi) pupae were examined. *P*-value by unpaired *t*-test. Genotypes: (**a** and **b**)
582 *MRLC^{AX3}/Y;MRLC-MRLC::GFP;AbdB-Gal4, UAS-H2B::ECFP/+* (Control) and
583 *MRLC^{AX3}/Y;MRLC-MRLC::GFP;AbdB-Gal4, UAS-H2B::ECFP/UAS-Pak3 RNAi*; (**c**–**e**)
584 *MRLC^{AX3}/Y;MRLC-MRLC::GFP/UAS-Lifeact::Ruby;AbdB-Gal4, UAS-H2B::ECFP/UAS-*
585 *Pak3 RNAi*; (**f** and **g**) *MRLC^{AX3}/Y;MRLC-MRLC::GFP/+;AbdB-Gal4, UAS-H2B::ECFP/UAS-*
586 *Pak3 RNAi* and *MRLC^{AX3}/Y;MRLC-MRLC::GFP/UAS-Abi RNAi;AbdB-Gal4, UAS-*
587 *H2B::ECFP/UAS-Pak3 RNAi*; (**h** and **i**) *+/Y;E-Cad::GFP;AbdB-Gal4, UAS-H2B::ECFP/+*

bioRxiv preprint doi: https://doi.org/10.1101/743237; this version posted August 22, 2019. The copyright holder for this preprint (which was not certified by peer review) is the author/funder, who has granted bioRxiv a license to display the preprint in perpetuity. It is made available under aCC-BY 4.0 International license.

(Control) and *+/Y;E-Cad::GFP;AbdB-Gal4, UAS-H2B::ECFP/UAS-Pak3 RNAi*.

Figure 4 | Reduction of E-cadherin levels at junctions induces myosin II dissociation. (**a**) Magnified time-lapse images of E-Cad::GFP at junctions. Arrowheads indicate E-Cad::GFP-positive protrusions, and broken lines indicate the local decrease in E-Cad::GFP levels at the bases of the protrusions. Scale bar, 3 μm. (**b** and **c**) Images of junctions with E-Cad::GFP and Lifeact::Ruby in control (b) and Pak3 RNAi (c) cells. Arrowheads indicate E-Cad::GFP and Lifeact::Ruby double-positive protrusions. Scale bar, 2 (b) and 3 (c) μm. (**d**) Schema of E-Cad::GFP intensities at local areas on the junctions with ($Int_{w/}$) and without ($Int_{w/o}$) large actin (magenta) protrusions. (**e**) Mean ± S.D. of the ratio of $Int_{w/}$ and $Int_{w/o}$ per junction. Parentheses indicate the number of examined junctions from 4 (Pak3 RNAi) and 3 (Pak3 RNAi and E-Cad::GFP overexpression) pupae. *P*-value by unpaired *t*-test. (**f**) Percentages of junctions forming large actin protrusions for the indicated number of times per hour are shown. Parentheses indicate the number of examined junctions from 4 pupae per genotype. *P*-values by Mann-Whitney *U*-test. (**g**) Representative images of split MRLC::GFP cables (orange arrowheads) at junctions. Scale bar, 5 μm. (**h**) Mean ± S.D. of the lengths of junctions with split myosin II cables. The Pak3 RNAi data (left) are the same as in Fig. 3g. Parenthesis indicates the number of examined junctions from 6 pupae. *P*-value by Dunnett's test.

bioRxiv preprint doi: https://doi.org/10.1101/743237; this version posted August 22, 2019. The copyright holder for this preprint (which was not certified by peer review) is the author/funder, who has granted bioRxiv a license to display the preprint in perpetuity. It is made available under aCC-BY 4.0 International license.

Genotypes: (**a**) *+/Y;E-Cad::GFP;AbdB-Gal4, UAS-H2B::ECFP/+* (Control) and *+/Y;E-Cad::GFP;AbdB-Gal4, UAS-H2B::ECFP/UAS-Pak3 RNAi*; (**b**) *+/Y;E-Cad::GFP/UAS-LifeAct::Ruby;AbdB-Gal4/+*; (**c** and **e**) *+/Y;E-Cad::GFP/UAS-Lifeact::Ruby;AbdB-Gal4/UAS-Pak3 RNAi* and *+/Y;Ubi-E-Cad::GFP/UAS-Lifeact::Ruby;AbdB-Gal4/UAS-Pak3 RNAi*; (**f**) *+/Y; UAS-Lifeact::Ruby/+;AbdB-Gal4/UAS-Pak3 RNAi* and *+/Y; UAS-Lifeact::Ruby/Ubi-E-Cad::GFP;AbdB-Gal4/UAS-Pak3 RNAi*; (**g** and **h**) $MRLC^{AX3}$*/Y;MRLC-MRLC::GFP/UAS-E-cadherin;AbdB-Gal4, UAS-H2B::ECFP/UAS-Pak3 RNAi.*

Figure 5 | E-cadherin overexpression rescues tissue dynamics. (**a**) Mean ± S.D. of the percentages of junctions with the categorized dynamics. Bar colors correspond to Fig. 1e. The Pak3 RNAi data (left) are the same as in Fig. 1f. Parenthesis indicates the number of examined junctions from 3 pupae per genotype. *P*-values by Tukey's test. (**b**) Percentages of male adult flies with genitalia angles indicated in Fig. 1b are shown. Parenthesis indicates the number of males examined. (**c**) Schema of Pak3-dependent junction contraction. (i)–(iv) indicate the negative feedback mechanism (green arrows, described in the Discussion section). Genotypes: (**a**) *+/Y;Ubi-E-Cad::GFP/E-Cad::GFP;AbdB-Gal4, UAS-H2B::ECFP/UAS-Pak3 RNAi*; (**b**) *+/Y;Ubi-E-Cad::GFP/+;AbdB-Gal4, UAS-H2B::ECFP/UAS-Pak3 RNAi.*

Supplementary Movie 1. Dynamics of cell–cell junctions during the movement of control

bioRxiv preprint doi: https://doi.org/10.1101/743237; this version posted August 22, 2019. The copyright holder for this preprint (which was not certified by peer review) is the author/funder, who has granted bioRxiv a license to display the preprint in perpetuity. It is made available under aCC-BY 4.0 International license.

622 A8a cells. E-cadherin was visualized with E-Cad::GFP. Scale bar, 10 μm. Genotype, *+/Y;E-*

623 *Cad::GFP;AbdB-Gal4, UAS-H2B::ECFP/+*.

624 **Supplementary Movie 2.** Dynamics of cell–cell junctions during the movement of Pak3 RNAi

625 A8a cells. E-cadherin was visualized with E-Cad::GFP. Scale bar, 10 μm. Genotype, *+/Y;E-*

626 *Cad::GFP;AbdB-Gal4, UAS-H2B::ECFP/UAS-Pak3 RNAi*.

627 **Supplementary Movie 3.** Dynamics of actin at cell–cell junctions in the control A8a cells.

628 Actin was visualized with Lifeact::GFP. Scale bar, 10 μm. Genotype, *+/Y;UAS-*

629 *Lifeact::GFP;AbdB-Gal4/+*.

630 **Supplementary Movie 4.** Dynamics of actin at cell–cell junctions in the Pak3 RNAi A8a cells.

631 Actin was visualized with Lifeact::GFP. Scale bar, 10 μm. Genotype, *+/Y;UAS-*

632 *Lifeact::GFP;AbdB-Gal4/UAS-Pak3 RNAi*.

633 **Supplementary Movie 5.** Dynamics of E-Cad::GFP at cell–cell junctions in the control A8a

634 cells. Scale bar, 3 μm. Genotype, *+/Y;E-Cad::GFP;AbdB-Gal4, UAS-H2B::ECFP/+*.

635 **Supplementary Movie 6.** Dynamics of E-Cad::GFP at cell–cell junctions in Pak3 RNAi A8a

636 cells. Scale bar, 3 μm. Genotype, *+/Y;E-Cad::GFP;AbdB-Gal4, UAS-H2B::ECFP/UAS-Pak3*

637 *RNAi*.

638

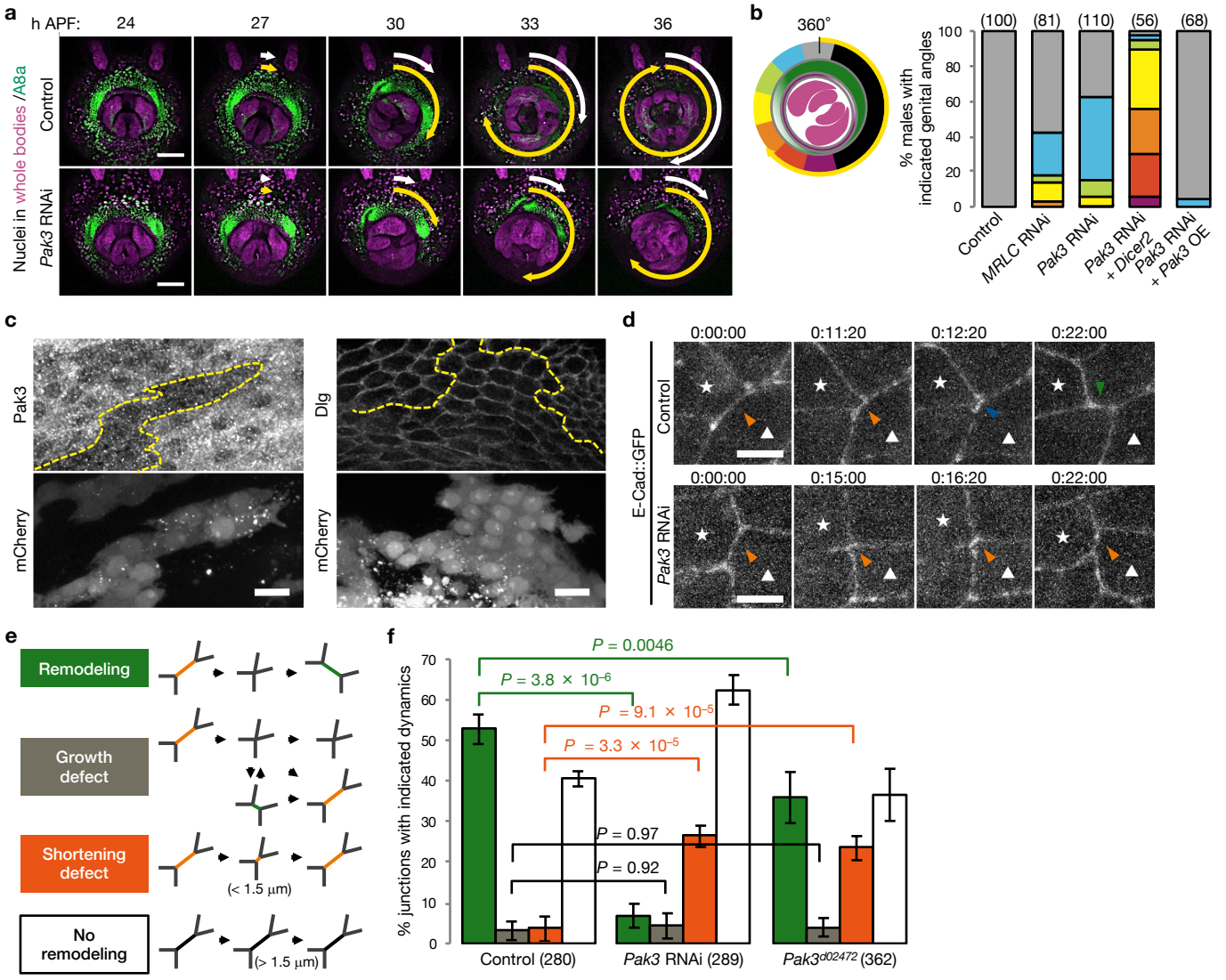
a
h APF:
24
27
30
33
36
Nuclei in whole bodies /A8a
Control
Pak3 RNAi
b
360°
% males with indicated genital angles
(100)
(81)
(110)
(56)
(68)
Control
MRLC RNAi
Pak3 RNAi
Pak3 RNAi + Dicer2
Pak3 RNAi + Pak3 OE
c
Pak3
mCherry
Dlg
mCherry
d
E-Cad::GFP
Control
Pak3 RNAi
0:00:00
0:11:20
0:12:20
0:22:00
0:00:00
0:15:00
0:16:20
0:22:00
e
Remodeling
Growth defect
Shortening defect
No remodeling
(< 1.5 μm)
(> 1.5 μm)
f
% junctions with indicated dynamics
P = 0.0046
P = 3.8 × 10−6
P = 9.1 × 10−5
P = 3.3 × 10−5
P = 0.97
P = 0.92
Control (280)
Pak3 RNAi (289)
Pak3d02472 (362)

Figure 1

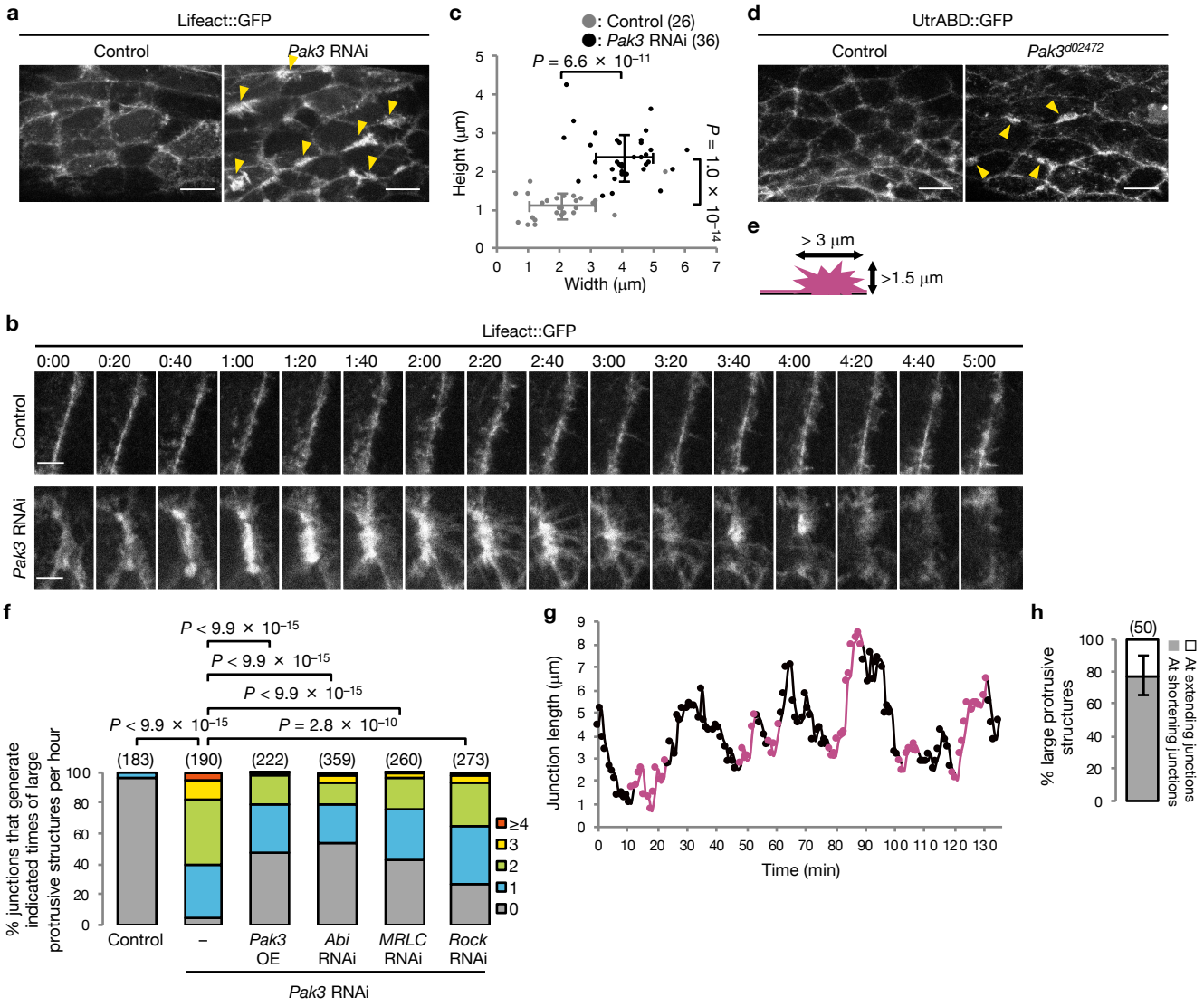
a
Lifeact::GFP
Control
Pak3 RNAi
c
●: Control (26)
●: Pak3 RNAi (36)
P = 6.6 × 10−11
P = 1.0 × 10−14
Height (μm)
Width (μm)
d
UtrABD::GFP
Control
Pak3d02472
e
> 3 μm
>1.5 μm
b
Lifeact::GFP
0:00 0:20 0:40 1:00 1:20 1:40 2:00 2:20 2:40 3:00 3:20 3:40 4:00 4:20 4:40 5:00
Control
Pak3 RNAi
f
P < 9.9 × 10−15
P < 9.9 × 10−15
P < 9.9 × 10−15
P < 9.9 × 10−15
P = 2.8 × 10−10
(183) (190) (222) (359) (260) (273)
% junctions that generate indicated times of large protrusive structures per hour
≥4
3
2
1
0
Control
–
Pak3 OE
Abi RNAi
MRLC RNAi
Rock RNAi
Pak3 RNAi
g
Junction length (μm)
Time (min)
h
(50)
% large protrusive structures
At extending junctions
At shortening junctions

Figure 2

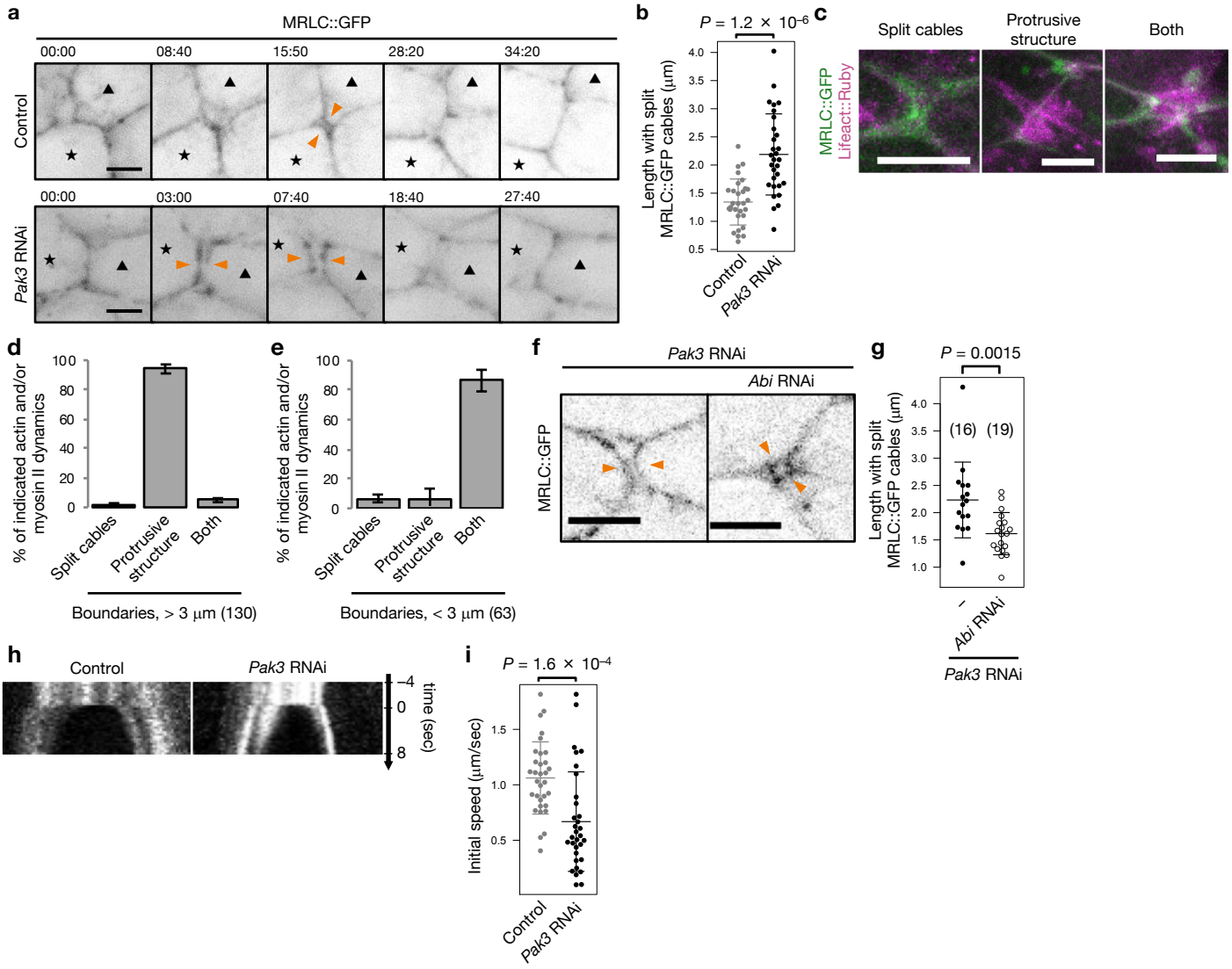
a
MRLC::GFP
00:00
08:40
15:50
28:20
34:20
Control
00:00
03:00
07:40
18:40
27:40
Pak3 RNAi
b
P = 1.2 × 10−6
Length with split MRLC::GFP cables (μm)
Control
Pak3 RNAi
c
Split cables
Protrusive structure
Both
MRLC::GFP
Lifeact::Ruby
d
% of indicated actin and/or myosin II dynamics
Split cables
Protrusive structure
Both
Boundaries, > 3 μm (130)
e
% of indicated actin and/or myosin II dynamics
Split cables
Protrusive structure
Both
Boundaries, < 3 μm (63)
f
Pak3 RNAi
Abi RNAi
MRLC::GFP
g
P = 0.0015
Length with split MRLC::GFP cables (μm)
(16)
(19)
–
Abi RNAi
Pak3 RNAi
h
Control
Pak3 RNAi
time (sec)
−4
0
8
i
P = 1.6 × 10−4
Initial speed (μm/sec)
Control
Pak3 RNAi

Figure 3

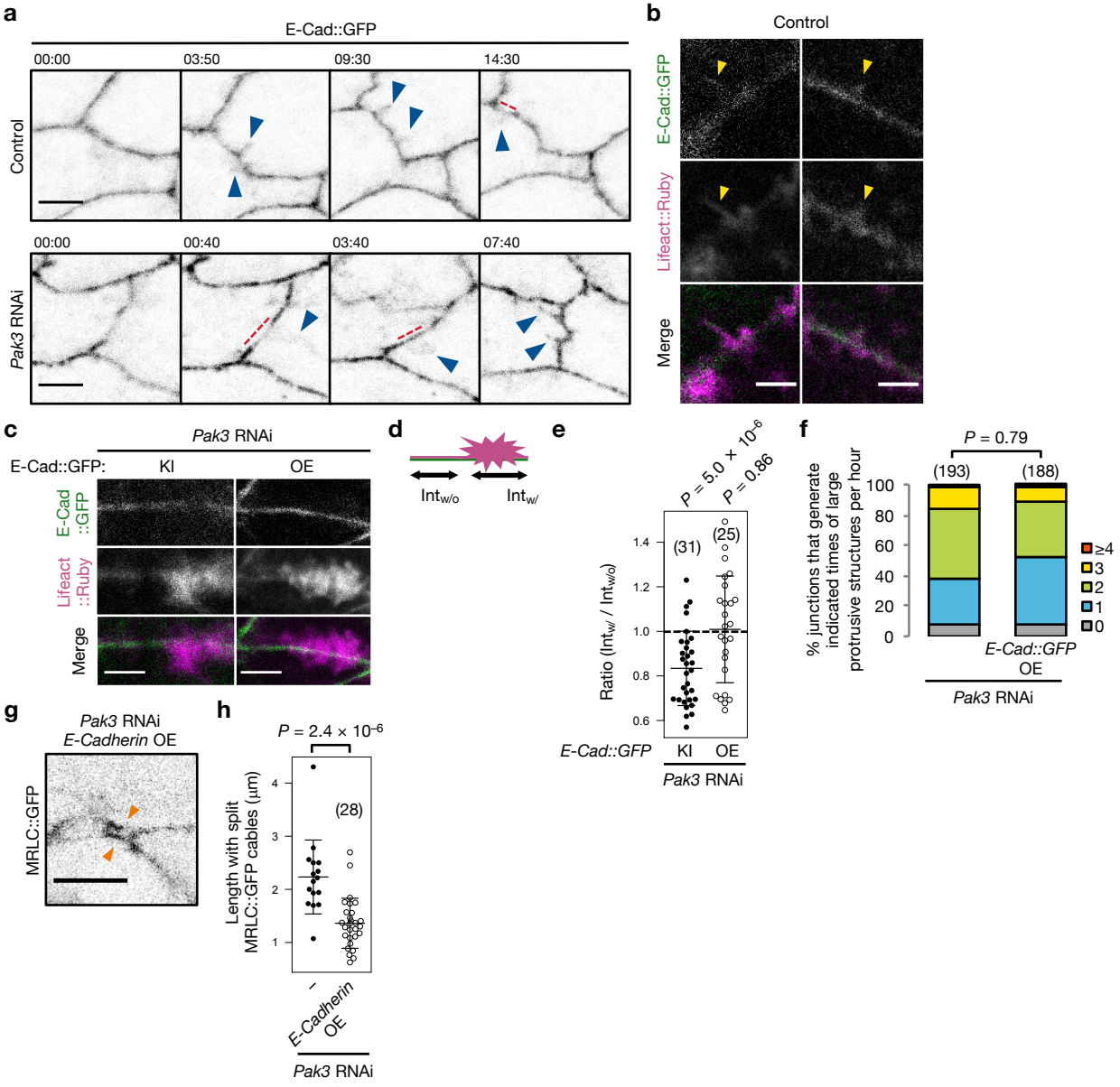
a
E-Cad::GFP
00:00
03:50
09:30
14:30
Control
00:00
00:40
03:40
07:40
Pak3 RNAi
b
Control
E-Cad::GFP
Lifeact::Ruby
Merge
c
Pak3 RNAi
E-Cad::GFP:
KI
OE
E-Cad ::GFP
Lifeact ::Ruby
Merge
d
Int w/o
Int w/
e
P = 5.0 × 10−6
P = 0.86
Ratio (Int w/ / Int w/o)
1.4
1.2
1.0
0.8
0.6
(31)
(25)
E-Cad::GFP
KI
OE
Pak3 RNAi
f
P = 0.79
(193)
(188)
% junctions that generate indicated times of large protrusive structures per hour
100
80
60
40
20
0
≥4
3
2
1
0
E-Cad::GFP
OE
Pak3 RNAi
g
Pak3 RNAi
E-Cadherin OE
MRLC::GFP
h
P = 2.4 × 10−6
Length with split MRLC::GFP cables (μm)
4
3
2
1
(28)
–
E-Cadherin OE
Pak3 RNAi

Figure 4

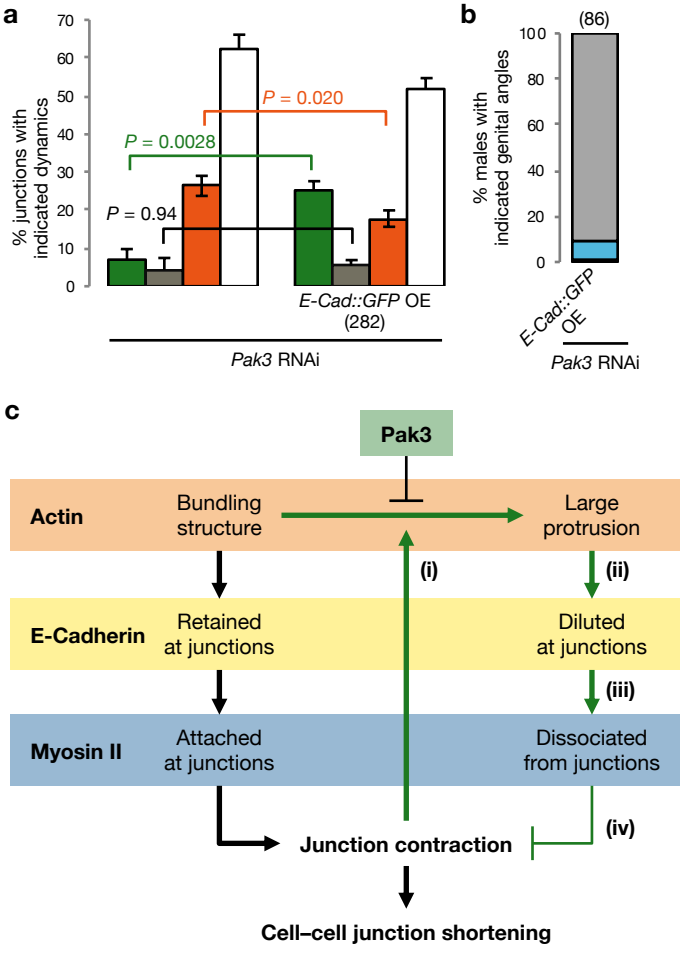
a
% junctions with indicated dynamics
70
60
50
40
30
20
10
0
P = 0.020
P = 0.0028
P = 0.94
E-Cad::GFP OE
(282)
Pak3 RNAi
b
% males with indicated genital angles
100
80
60
40
20
0
(86)
E-Cad::GFP OE
Pak3 RNAi
c
Pak3
Actin
Bundling structure
Large protrusion
(i)
(ii)
E-Cadherin
Retained at junctions
Diluted at junctions
(iii)
Myosin II
Attached at junctions
Dissociated from junctions
(iv)
Junction contraction
Cell–cell junction shortening

Figure 5